XLVI CILAMCE
VITÓRIA - ES - BRAZIL - 2025
XLVI IBERO-LATIN AMERICAN CONGRESS ON COMPUTATIONAL METHODS IN ENGENEERING

Full-Waveform Reconstruction of Microseismic Sources From Hydroacoustic Observations

Welerson F. Kneipp[1,2], Antonio A. Novotny[1], Bojan B. Guzina[3]

[1]*Coordenação de Métodos Matemáticos e Computacionais, Laboratório Nacional de Computação Científica*
Av. Getúlio Vargas 333, 25651-075 Petrópolis - RJ, Brasil
welerson@posgrad.lncc.br, novotny@lncc.br
[2]*Coordenação de Licenciatura em Matemática, Centro Federal de Educação Tecnológica Celso S. da Fonseca*
Rua do Imperador 971, 25620-003, Petrópolis - RJ, Brasil
welerson.kneipp@cefet-rj.br
[3]*Department of Civil, Environmental, and Geo-Engineering, University of Minnesota*
Minneapolis, MN 55455, United States
guzin001@umn.edu

Abstract. This work presents a full-waveform inversion strategy for identifying microseismic events in coupled solid–fluid systems based on multi-frequency acoustic pressure measurements collected in the fluid. The goal is to reconstruct both the spatial locations and seismic moment tensors of the events, motivated by applications such as the monitoring of reaction-induced fracturing in subsurface carbon storage formations. The microseismic sources are modeled as dipole and double-couple point forces embedded within the solid region. The inversion procedure relies on a topological derivative approach, where the leading-order perturbation of a misfit functional reflects the elastic energy released by the nucleation of an infinitesimal crack at a trial location. The forward problem is formulated in the frequency domain, coupling linear elastodynamics in the solid and acoustic wave propagation in the surrounding fluid. The algorithm combines discrete grid search, adaptive refinement, and spectral data assimilation. Numerical simulations in two dimensions validate the ability to reconstruct multiple sources using a modest number of hydrophones and reveal the trade-off between spatial and spectral aperture.

Keywords: Microseismic event reconstruction, full-waveform analysis, seismic moment tensor, hydrophones

1 Introduction

Accurate reconstruction of microseismic events, in terms of their location and kinematic discontinuity characteristics, is of critical importance in seismology, reservoir engineering, geomechanics, and the monitoring of geological CO_2 storage [1, 2]. This reconstruction is effected via interpretation of the resulting seismic motion, also known as acoustic emission (AE). While classical AE inversion techniques [3, 4] offer coarse localization, they often fall short in resolving the rupture mode. A more faithful characterization is achieved via the seismic moment tensor [5, 6], which synthesizes the mechanics of a point-like displacement discontinuity associated with a micro-fracture surface.

Full-waveform inversion (FWI) has emerged as a powerful strategy that leverages the entirety of recorded waveforms to reconstruct both the spatial and kinematic features of AE sources [7, 8]. Most existing techniques, however, rely on particle motion data acquired via accelerometers or geophones, which may be impractical in certain experimental or fluid-rich environments [9].

A promising alternative lies in the use of hydrophones—acoustic pressure sensors—which have demonstrated utility in AE localization within fluid-filled boreholes [10], structural monitoring of pipelines [11], and failure detection in submerged systems [12]. From an experimental perspective, hydrophones couple seamlessly with the fluid and offer broad spectral response, rendering them suitable for both low- and high-frequency regimes.

Recent works [13, 14] have proposed frequency-domain FWI techniques based on motion data collected at solid boundaries. Building upon these ideas, the present study introduces a coupled solid–fluid framework and proposes a new sensing strategy based exclusively on hydroacoustic pressure traces. Motivated by the prospect of reaction-induced fracturing in mineralization-driven carbon storage systems [15, 16], we investigate the viability of reconstructing both the locations and seismic moment tensors of AE sources using frequency-domain hydrophone observations.

2 Problem formulation

Consider a two-phase domain $\Omega = \boldsymbol{x} \in \mathbb{R}^2 : \boldsymbol{x} \cdot \boldsymbol{e}_2 > 0$ composed of an elastic solid region Ω_s and an inviscid fluid region $\Omega_\mathrm{f} = \Omega \setminus \Omega_\mathrm{s}$, as shown in Fig. 1. The interface between the subdomains is denoted by $\Gamma = \partial\Omega_\mathrm{s} \setminus \Sigma$, and $\Sigma = \partial\Omega$ represents the boundary exposed to radiation conditions. Let $\boldsymbol{e}_j$ $(j = 1, 2)$ denote the Cartesian basis, and adopt Einstein's convention over repeated indices.

Let $\boldsymbol{u} : \Omega_\mathrm{s} \to \mathbb{C}^2$ be the solid displacement, $\boldsymbol{\sigma} : \Omega_\mathrm{s} \to \mathbb{C}^{2\times2}$ the stress tensor, and $p : \Omega_\mathrm{f} \to \mathbb{C}$ the pressure field in the fluid. The stress tensor is given by

$$\boldsymbol{\sigma} = \lambda(\nabla \cdot \boldsymbol{u})\boldsymbol{I} + \mu(\nabla\boldsymbol{u} + \nabla^\mathrm{T}\boldsymbol{u}), \tag{1}$$

where $\lambda = K - \frac{2}{3}\mu$ is the first Lamé parameter. The material constants (K, μ, ρ) and (κ, ϱ) respectively denote the bulk modulus, shear modulus, and density of the solid and fluid. Assuming time-harmonic fields with implicit factor $e^{-i\omega t}$, and acoustic pressure measurements taken at discrete fluid locations $\Theta_\mathrm{obs} = \boldsymbol{x}_\mathfrak{m} \in \Omega_\mathrm{f}, ; \mathfrak{m} = \overline{1, M}$, we are interested in the *inverse source problem* of reconstructing the source density $\widehat{\boldsymbol{f}}$ from discrete observations, p^obs, of acoustic pressure in the fluid that are connected via the forward map

$$\begin{cases} \nabla\cdot\boldsymbol{\sigma} + \rho\omega^2\boldsymbol{u} &= -\widehat{\boldsymbol{f}} \quad \text{in} \quad \Omega_\mathrm{s}, \\ \nabla^2 p + k_\mathrm{f}^2 p &= 0 \quad \text{in} \quad \Omega_\mathrm{f}, \\ (\nabla p + \varrho\omega^2\boldsymbol{u})\cdot\boldsymbol{n} &= 0 \quad \text{on} \quad \Gamma, \\ \boldsymbol{\sigma}\cdot\boldsymbol{n} + p\boldsymbol{n} &= \boldsymbol{0} \quad \text{on} \quad \Gamma, \\ \boldsymbol{u} &= \boldsymbol{0} \quad \text{on} \quad \partial\Omega_\mathrm{s} \cap \Sigma, \\ \nabla p\cdot\boldsymbol{\nu} &= 0 \quad \text{on} \quad \partial\Omega_\mathrm{f} \cap \Sigma, \\ \lim_{r\to\infty} r^{\frac{1}{2}}(\partial/\partial r - ik_\mathrm{f})p &= 0 \quad \text{on} \quad \Xi_r, \\ p &= p^\mathrm{obs} \quad \text{in} \quad \Theta_\mathrm{obs}, \end{cases} \tag{2}$$

where $k_\mathrm{f} = \omega\sqrt{\varrho/\kappa}$ and $r = |\boldsymbol{x}|$.

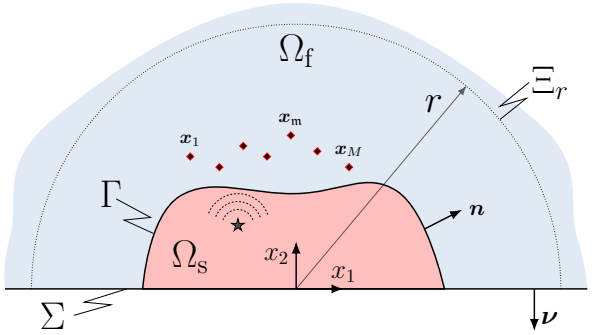


Figure 1. Problem setting featuring a solid body (Ω_s) subject to a microseismic event "$\star$" and measurements of the so-generated acoustic pressure fluctuations in the surrounding semi-infinite fluid (Ω_f) over a set of discrete locations $\boldsymbol{x}_\mathfrak{m}$, $\mathfrak{m} = \overline{1, M}$.

2.1 Representation of the microseismic events

Motivated by laboratory applications and the transient nature of microseismic events, we represent the true source density $\widehat{\boldsymbol{f}}$ as a superposition of a finite number of dipoles and double couples [5, 6], each modulated by a frequency-dependent amplitude. In particular, we assume that $\widehat{\boldsymbol{f}} \in C_\delta(\Omega_\mathrm{s})$, with

$$C_\delta(\Omega_\mathrm{s}) = \Big\{ \boldsymbol{f} \colon \Omega_\mathrm{s} \to \mathbb{C}^2 \mid \boldsymbol{f}(\boldsymbol{x};\omega_j) = \sum_{n=1}^{N} \breve{S}^{(n)}_{\tau_n}(\omega_j)\, \boldsymbol{M}^{(n)} \cdot \nabla_{\boldsymbol{x}^{(n)}} \delta(\boldsymbol{x} - \boldsymbol{x}^{(n)}),\ \boldsymbol{x}^{(n)} \in \Omega_\mathrm{s} \Big\}, \tag{3}$$

where $\delta(\cdot)$ denotes the two-dimensional Dirac delta function; N is the number of sources located at $\boldsymbol{x}^{(n)} \in \Omega_\mathrm{s}$ $(n = \overline{1, N})$, and $\boldsymbol{M}^{(n)} \in \mathbb{R}^{2\times2}$ are symmetric seismic moment tensors [6]. The modulation functions $\breve{S}^{(n)}_{\tau_n}(\omega_j)$ arise from the Fourier transform of time-localized waveforms $S^{(n)}(t - \tau_n)$. Each $S^{(n)}(t)$ is taken as a Morlet wavelet:

$$S^{(n)}(t) = a_n e^{-(t/\varsigma_n)^2} \cos(\omega^{(n)} t), \tag{4}$$

where a_n is the amplitude, ς_n the temporal aperture, and $\omega^{(n)}$ the center frequency. Its Fourier transform is

$$\breve{S}^{(n)}(\omega) = \tfrac{\sqrt{2}}{4} a_n \varsigma_n \, \exp\left(-\tfrac{1}{4}\varsigma_n^2(\omega^{(n)} + \omega)^2\right)\left(1 + e^{\varsigma_n^2\omega^{(n)}\omega}\right), \tag{5}$$

with the time shift τ_n included via

$$\breve{S}^{(n)}_{\tau_n}(\omega) = \breve{S}^{(n)}(\omega)\, e^{i\omega\tau_n}. \tag{6}$$

The sampling frequencies ω_j ($j = \overline{1, J}$) are chosen to capture the spectral content of the microseismic events. The multifrequency source representation $\boldsymbol{f}(\boldsymbol{x}; \omega_j)$ thus encodes both the spatial and spectral characteristics of the transient sources. On the basis of (3), we represent the true source density featured by (2) as

$$\widehat{\boldsymbol{f}}(\boldsymbol{x}; \omega_j) = \sum_{n=1}^{\widehat{N}} \breve{S}_{\tau_n}^{(n)}(\omega_j)\, \widehat{\boldsymbol{M}}^{(n)} \cdot \nabla_{\boldsymbol{x}^{(n)}} \delta(\boldsymbol{x} - \widehat{\boldsymbol{x}}^{(n)}). \tag{7}$$

In this setting, our task consists in reconstructing $\widehat{\boldsymbol{f}} \in C_\delta(\Omega_\mathrm{s})$ in terms of the microseismic event locations $\widehat{\boldsymbol{x}}^{(n)}$ and moment tensors $\widehat{\boldsymbol{M}}^{(n)}$, given $S^{(n)}$, from M pointwise pressure measurements p^obs taken over Θ_obs. Assuming the inverse problem derived from (2) and (7) to be algebraically over-determined, we formulate it as a constrained optimization problem. Specifically, we introduce the multi-frequency cost functional

$$\mathcal{J}(\boldsymbol{p}) = \mathcal{J}(p_1, \ldots, p_J) = \tfrac{1}{2} \sum_{j=1}^{J} \int_{\Omega_\mathrm{f}} \mathfrak{s}(\boldsymbol{x}) (p_j - p_j^\mathrm{obs}) \overline{(p_j - p_j^\mathrm{obs})}\, \mathrm{d}\Omega_\mathrm{f}, \tag{8}$$

where the overbar denotes complex conjugation, the function $\mathfrak{s}(\boldsymbol{x})$ is given by

$$\mathfrak{s}(\boldsymbol{x}) = \sum_{\mathfrak{m}=1}^{M} \delta(\boldsymbol{x} - \boldsymbol{x}_\mathfrak{m}^\mathrm{obs}), \tag{9}$$

and $p_j(\cdot; \boldsymbol{f}) : \Omega_\mathrm{f} \mapsto \mathbb{C}$ solves the coupled boundary value problem

$$\left\{ \begin{array}{rcll} \nabla \cdot \boldsymbol{\sigma}_j + \rho \omega_j^2 \boldsymbol{u}_j &=& -\boldsymbol{f}(\boldsymbol{x}; \omega_j) & \text{in} \quad \Omega_\mathrm{s}, \\ \nabla^2 p_j + k_{\mathrm{f}j}^2 p_j &=& 0 & \text{in} \quad \Omega_\mathrm{f}, \\ (\nabla p_j + \varrho \omega_j^2 \boldsymbol{u}_j) \cdot \boldsymbol{n} &=& 0 & \text{on} \quad \Gamma, \\ \boldsymbol{\sigma}_j \cdot \boldsymbol{n} + p_j \boldsymbol{n} &=& \boldsymbol{0} & \text{on} \quad \Gamma, \\ \boldsymbol{u}_j &=& \boldsymbol{0} & \text{on} \quad \partial\Omega_\mathrm{s} \cap \Sigma, \\ \nabla p_j \cdot \boldsymbol{\nu} &=& 0 & \text{on} \quad \partial\Omega_\mathrm{f} \cap \Sigma, \\ \lim_{r \to \infty} r^{\frac{1}{2}} \left(\frac{\partial}{\partial r} - i k_{\mathrm{f}j} \right) p_j &=& 0 & \text{on} \quad \Xi_r. \end{array} \right. \tag{10}$$

In this setting, we reformulate the above inverse problem as an optimization problem of the form

$$\underset{\boldsymbol{f} \in C_\delta(\Omega_\mathrm{s})}{\text{Minimize}}\ \mathcal{J}(p_1, \ldots, p_J), \quad \text{subject to (10)}. \tag{11}$$

2.2 Sensitivity analysis

In order to proceed with the minimization of the cost functional (8), we consider a perturbation of the trial source term $\boldsymbol{f} \in C_\delta(\Omega_\mathrm{s})$ in (10) by a prescribed number N of point sources. Specifically, for each sampled frequency ω_j ($j = \overline{1, J}$), we define the perturbed source as

$$\tilde{\boldsymbol{f}}(\boldsymbol{x}; \omega_j) = \boldsymbol{f}(\boldsymbol{x}; \omega_j) + \sum_{n=1}^{N} \breve{S}_{\tau_n}^{(n)}(\omega_j)\, \boldsymbol{M}^{(n)} \cdot \nabla_{\boldsymbol{x}^{(n)}} \delta(\boldsymbol{x} - \boldsymbol{x}^{(n)}). \tag{12}$$

From (10) and (12), the perturbed forward solutions $\tilde{\boldsymbol{u}}_j : \Omega_\mathrm{s} \to \mathbb{C}^2$ (in the solid) and $\tilde{p}_j : \Omega_\mathrm{f} \to \mathbb{C}$ (in the fluid) satisfying similar equation to (10). The corresponding perturbed multi-frequency cost functional reads

$$\mathcal{J}(\tilde{p}_1, \ldots, \tilde{p}_J) = \tfrac{1}{2} \sum_{j=1}^{J} \int_{\Omega_f} \mathfrak{s}(\boldsymbol{x}) \left(\tilde{p}_j - p_j^\mathrm{obs} \right) \overline{\left(\tilde{p}_j - p_j^\mathrm{obs} \right)}\, \mathrm{d}\Omega_\mathrm{f}. \tag{13}$$

Assuming an upper bound N on the number of events located at trial points $\boldsymbol{x}^{(n)}$, $n = \overline{1, N}$, we seek to evaluate the variation of the cost functional (8) with respect to the components of the moment tensors at each candidate location, for this purpose, we deploy the dyadic representation $\boldsymbol{M}^{(n)} = M_{kl}^{(n)} \boldsymbol{e}_k \otimes \boldsymbol{e}_l, k, l = \overline{1, 2}$. Featuring the scalar coefficients $M_{kl}^{(n)} \in \mathbb{R}$, the perturbed solutions can be conveniently written as

$$\tilde{u}_j(\boldsymbol{x}) = u_j(\boldsymbol{x}) + \sum_{n=1}^{N} \breve{S}_{\tau_n}^{(n)}(\omega_j)\, M_{kl}^{(n)}\, v_{kl,i}^{(n,j)}(\boldsymbol{x}) \tag{14}$$

$$\tilde{p}_j(\boldsymbol{x}) = p_j(\boldsymbol{x}) + \sum_{n=1}^{N} \breve{S}_{\tau_n}^{(n)}(\omega_j)\, M_{kl}^{(n)}\, q_{kl}^{(n,j)}(\boldsymbol{x}), \tag{15}$$

where $v_{kl}^{(n,j)}$ and $q_{kl}^{(n,j)}$ solve the respective canonical problems

$$\left\{\begin{array}{rcll} \nabla\cdot\boldsymbol{\sigma}_{kl}^{(n,j)} + \rho\omega_j^2\boldsymbol{v}_{kl}^{(n,j)} &=& -\boldsymbol{f}_{kl}^{(n)} & \text{in } \Omega_{\mathrm{s}}, \\ \nabla^2 q_{kl}^{(n,j)} + k_{\mathrm{f}_j}^2 q_{kl}^{(n,j)} &=& 0 & \text{in } \Omega_{\mathrm{f}}, \\ (\nabla q_{kl}^{(n,j)} + \varrho\omega_j^2\boldsymbol{v}_{kl}^{(n,j)})\cdot\boldsymbol{n} &=& 0 & \text{on } \Gamma, \\ \boldsymbol{\sigma}_{kl}^{(n,j)}\cdot\boldsymbol{n} + q_{kl}^{(n,j)}\boldsymbol{n} &=& \boldsymbol{0} & \text{on } \Gamma, \\ \boldsymbol{v}_{kl}^{(n,j)} &=& \boldsymbol{0} & \text{on } \partial\Omega_{\mathrm{s}}\cap\Sigma, \\ \nabla q_{kl}^{(n,j)}\cdot\boldsymbol{\nu} &=& 0 & \text{on } \partial\Omega_{\mathrm{f}}\cap\Sigma, \\ \lim_{r\to\infty} r^{1/2}\left(\frac{\partial}{\partial r} - ik_{\mathrm{f}_j}\right) q_{kl}^{(n,j)} &=& 0 & \text{on } \Xi_r, \end{array}\right. \tag{16}$$

with $\quad \boldsymbol{f}_{kl}^{(n)}(\boldsymbol{x}) = (\boldsymbol{e}_k\otimes\boldsymbol{e}_l)\cdot\nabla_{\boldsymbol{x}^{(n)}}\delta(\boldsymbol{x}-\boldsymbol{x}^{(n)})$.

For a set of canonical pressure solutions $q_{kl}^{(n,j)}$ $(k,l=\overline{1,2})$, we conveniently introduce an auxiliary set of single-index mappings $\mathrm{q}_\ell^{(n,j)}\colon \Omega_{\mathrm{f}}\mapsto\mathbb{R}$ $(\ell=\overline{1,3})$ given by

$$\mathrm{q}_1^{(n,j)} = q_{11}^{(n,j)}, \qquad \mathrm{q}_2^{(n,j)} = q_{22}^{(n,j)}, \qquad \mathrm{q}_3^{(n,j)} = q_{12}^{(n,j)} + q_{21}^{(n,j)}. \tag{17}$$

On substituting (15) into (13), and considering $\Psi(\boldsymbol{\alpha}) := \mathcal{J}(\tilde{p}_1,\ldots,\tilde{p}_J) - \mathcal{J}(p_1,\ldots,p_J)$, we obtain

$$\Psi(\boldsymbol{\alpha}) = \boldsymbol{d}\cdot\boldsymbol{\alpha} + \tfrac{1}{2}\boldsymbol{H}\boldsymbol{\alpha}\cdot\boldsymbol{\alpha}, \tag{18}$$

where

$$\boldsymbol{\alpha} = (\boldsymbol{\alpha}^{(1)},\boldsymbol{\alpha}^{(2)},\ldots,\boldsymbol{\alpha}^{(N)})^{\mathrm{T}}\in\mathbb{R}^{3N}, \quad \text{whit} \quad \boldsymbol{\alpha}^{(n)} = (M_{11}^{(n)}, M_{22}^{(n)}, M_{12}^{(n)})^{\mathrm{T}}, \tag{19}$$

and the vector $\boldsymbol{d}\in\mathbb{R}^{3N}$ and the matrice $\boldsymbol{H}\in\mathbb{R}^{3N\times 3N}$ are given respectively by

$$\boldsymbol{d} = \begin{pmatrix} d^{(1)} \\ d^{(2)} \\ \vdots \\ d^{(N)} \end{pmatrix} \qquad \text{and} \qquad \boldsymbol{H} = \begin{pmatrix} H^{(11)} & H^{(12)} & \ldots & H^{(1N)} \\ H^{(21)} & H^{(22)} & \ldots & H^{(2N)} \\ \vdots & \vdots & \ddots & \vdots \\ H^{(N1)} & H^{(N2)} & \ldots & H^{(NN)} \end{pmatrix}, \tag{20}$$

with the components of $h^{(n)}\in\mathbb{R}^3$ and $H^{(mn)}\in\mathbb{R}^{3\times 3}$ $(m,n=\overline{1,N})$ defined as

$$d_\ell^{(n)} = \sum_{j=1}^{J}\int_{\Omega_{\mathrm{f}}} \mathfrak{s}(\boldsymbol{x})\,\mathrm{Re}\left\{\breve{S}_{\tau_n}^{(n)}(\omega_j)\,\mathrm{q}_\ell^{(n,j)}\,\overline{(p_j - p_j^{\mathrm{obs}})}\right\}\mathrm{d}\Omega_{\mathrm{f}}, \quad \ell=\overline{1,3}, \tag{21}$$

$$H_{\ell\kappa}^{(mn)} = \sum_{j=1}^{J}\int_{\Omega_{\mathrm{f}}} \mathfrak{s}(\boldsymbol{x})\,\mathrm{Re}\left\{\breve{S}_{\tau_n}^{(n)}(\omega_j)\,\overline{\breve{S}_{\tau_m}^{(m)}(\omega_j)}\,\mathrm{q}_\ell^{(m,j)}\,\overline{\mathrm{q}_\kappa^{(n,j)}}\right\}\mathrm{d}\Omega_{\mathrm{f}}, \quad \ell,\kappa=\overline{1,3}. \tag{22}$$

2.3 Reconstruction algorithm

Note that $\Psi(\boldsymbol{\alpha})$ in (18) is a quadratic form with respect to the strength vectors $\boldsymbol{\alpha}$. From the optimality conditions written in terms of $\boldsymbol{\alpha}$, for each vector of *trial* source locations $\boldsymbol{\xi} = (\boldsymbol{x}^{(1)},\boldsymbol{x}^{(2)},\ldots,\boldsymbol{x}^{(N)})^{\mathrm{T}}\in\mathbb{R}^{2N}$, we obtain

$$\boldsymbol{\alpha}(\boldsymbol{\xi}) = -\boldsymbol{H}^{-1}\boldsymbol{d}. \tag{23}$$

On substituting (23) into (18), we thus arrive at a minimization problem with respect to the set locations $\boldsymbol{\xi}$, namely

$$\boldsymbol{\xi}^\star = \underset{\boldsymbol{\xi}\subset X}{\mathrm{argmin}}\left\{\Psi(\boldsymbol{\alpha}(\boldsymbol{\xi})) = \tfrac{1}{2}\boldsymbol{d}\cdot\boldsymbol{\alpha}(\boldsymbol{\xi})\right\}. \tag{24}$$

In what follows, we pursue (24) via a combinatorial search over a prescribed grid X of trial source locations as described in Algorithm 1, where Π maps the vector of nodal indices $(n_1,n_2,\cdots,n_N)$ into the corresponding vector of event locations $\boldsymbol{\xi} = (\boldsymbol{x}^{(n_1)},\boldsymbol{x}^{(n_2)},\ldots,\boldsymbol{x}^{(n_N)})^{\mathrm{T}}$, selected from the card$\{X\}$ admissible grid positions.

Algorithm 1: Multi-frequency reconstruction of N microseismic events

1: **Input:** N, X, $\boldsymbol{H}$, $\boldsymbol{S}$, $\boldsymbol{g}$, $\boldsymbol{h}$, S;
2: **Initialize:** $\Psi^\star\leftarrow\infty$, $\boldsymbol{\xi}^\star\leftarrow\boldsymbol{0}$, $\boldsymbol{\alpha}^\star\leftarrow\boldsymbol{0}$
3: **for** each N-tuple $(x^{(1)},\ldots,x^{(N)})\in X^N$ with distinct entries **do**
4: Set $\boldsymbol{\xi}\leftarrow(x^{(1)},\ldots,x^{(N)})$
5: Assemble vector $\boldsymbol{d}(\boldsymbol{\xi})$ and Hessian $\boldsymbol{H}(\boldsymbol{\xi})$
6: Solve $\boldsymbol{H}\,\boldsymbol{\alpha} = -\boldsymbol{d}$
7: Compute $\Psi(\boldsymbol{\alpha}(\boldsymbol{\xi})) = \frac{1}{2}\boldsymbol{d}\cdot\boldsymbol{\alpha}(\boldsymbol{\xi})$
8: **if** $\Psi(\boldsymbol{\alpha}) < \Psi^\star$ **then**
9: Update $\Psi^\star\leftarrow\Psi(\boldsymbol{\alpha})$, $\boldsymbol{\xi}^\star\leftarrow\boldsymbol{\xi}$, $\boldsymbol{\alpha}^\star\leftarrow\boldsymbol{\alpha}$
10: **end if**
11: **end for**
12: **Output:** Optimal event configuration $(\boldsymbol{\xi}^\star,\boldsymbol{\alpha}^\star)$, with minimized cost $\Psi^\star$

3 Numerical results

In the ensuing examples, we aim to reconstruct microseismic events in a square solid block shown in Fig. 2 with $\ell = 0.16$ m, made of sandstone with bulk modulus $K = 13$ GPa, shear modulus $\mu = 8$ GPa, and mass density $\rho = 2300\,\text{kg/m}^3$. The block is immersed in a semi-infinite body of water with mass density $\varrho = 1000\,\text{kg/m}^3$ and sound speed $c_\text{f} = \sqrt{\kappa/\varrho} = 1490$ m/s. Sensing locations are restricted to $\Theta_\text{obs} \subset \Omega_\text{obs} = \{\boldsymbol{x} \in \Omega_\text{f} : 0 < d(\boldsymbol{x}) \leq \ell\}$. The sampled AE frequencies used for source reconstruction are assumed to be in the range

$$\frac{\omega \ell}{\sqrt{\mu/\rho}} \in \left[\tfrac{20}{3}, \tfrac{40}{3}\right]\pi, \tag{25}$$

i.e. the linear frequencies of acoustic emission $\omega/(2\pi) \approx (40 \div 80)$kHz.

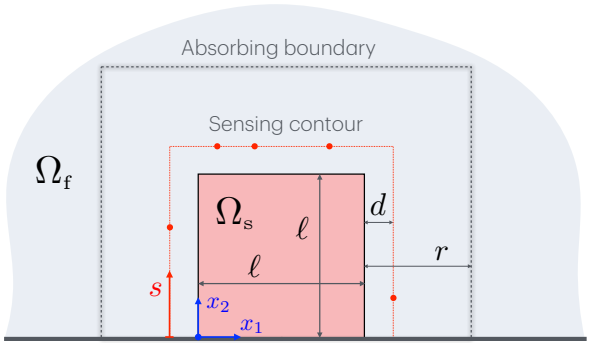


Figure 2. Testing setup used for numerical simulations

All simulations are performed in FreeFEM [17], using uniform triangular meshes with at least $12 \div 24$ elements per wavelength in the solid, and $10 \div 20$ in the fluid. To approximate (7), the two-dimensional Dirac gradient is described in terms of Gaussian distribution as

$$\nabla_{\boldsymbol{x}^{(n)}} \delta(\boldsymbol{x} - \boldsymbol{x}^{(n)}) = \left(\frac{\boldsymbol{x} - \boldsymbol{x}^{(n)}}{2\pi h^4}\right) \exp\left(-\frac{\|\boldsymbol{x} - \boldsymbol{x}^{(n)}\|^2}{2h^2}\right), \tag{26}$$

$h = h^e$, where h^e is the size of the finite element. To alleviate the "inverse crime", sensory data are generated in a larger domain ($r/\ell = 32$) and reconstructed with $r/\ell = 16$, yielding a controlled modeling mismatch of approximately 1%.

The transient nature of the sources is modeled using Morlet wavelets, whose parameters for the three distinct events (shear, tensile, and isotropic) used throughout our study are detailed in Table 1.

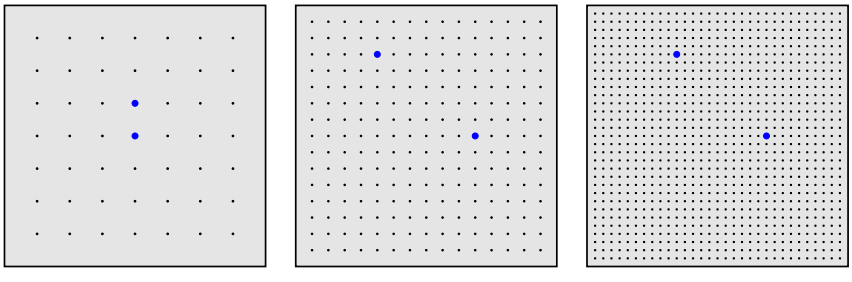
Table 1. Wavelet parameters of the contemporaneous transient events.

n	event	$\omega^{(n)}$	ς_n	a_n	τ_n
1	shear	$2\pi \times 61$kHz	28μs	1.6	22μs
2	tensile	$2\pi \times 54$kHz	25μs	2.1	0μs
3	isotropic	$2\pi \times 68$kHz	34μs	2.5	5μs

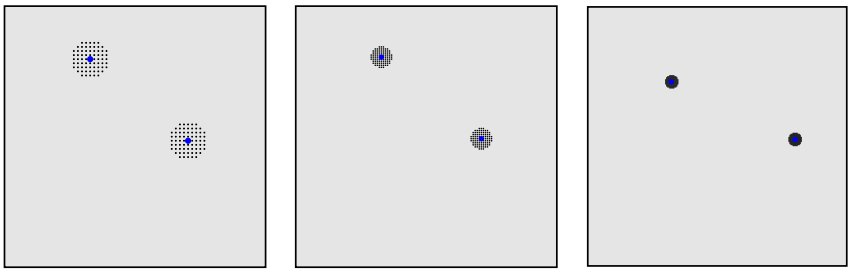
As a preliminary validation, we consider an on-grid scenario ($\widehat{\boldsymbol{\xi}} \subset X$), where the three transient events from Table 1 are reconstructed. Using sparse sensing configurations with (a) two sensors and four frequencies, and (b) a single sensor and eight frequencies, the algorithm successfully recovers both the source locations and their moment tensors. These results, omitted here for brevity, demonstrate the effectiveness of the method and provide a basis for more realistic off-grid and noisy reconstructions.

3.1 Adaptive search for off-grid events

To accurately locate sources that do not lie on the initial coarse grid ($\widehat{\boldsymbol{\xi}} \not\subset X$), we employ a two-stage adaptive grid refinement strategy. First, a sequence of global uniform refinements is performed to identify a stable coarse estimate of the source locations. Once such a solution is found, local non-uniform refinements are applied in the vicinity of the estimated positions to achieve high-resolution recovery. This separation ensures that local refinements are only performed once the global estimate is stable enough to avoid spurious convergence. Figure 3 illustrates this process for a noise-free case involving two off-grid events and six hydrophones. It shows two global refinement steps (a–c), followed by three local refinement steps (d–f), progressively converging to the true source locations. The final reconstructed parameters, reported in Table 2, confirm the accuracy and robustness of the adaptive procedure.



(a) X_1 and $\boldsymbol{\xi}_1^\star$ (b) X_2 and $\boldsymbol{\xi}_2^\star$ (c) X_3 and $\boldsymbol{\xi}_3^\star$



(d) X_4' and $\boldsymbol{\xi}_4^{\star\prime}$ (e) X_5' and $\boldsymbol{\xi}_5^{\star\prime}$ (f) X_6' and $\boldsymbol{\xi}_6^{\star\prime}$

Figure 3. Off-grid events, noise-free data: global (a–c) and local (d–f) grid search refinements.

Table 2. Off-grid events, noise-free data: "true" and reconstructed event parameters using six sensors and four sampled frequencies, after three global and seven local grid refinements.

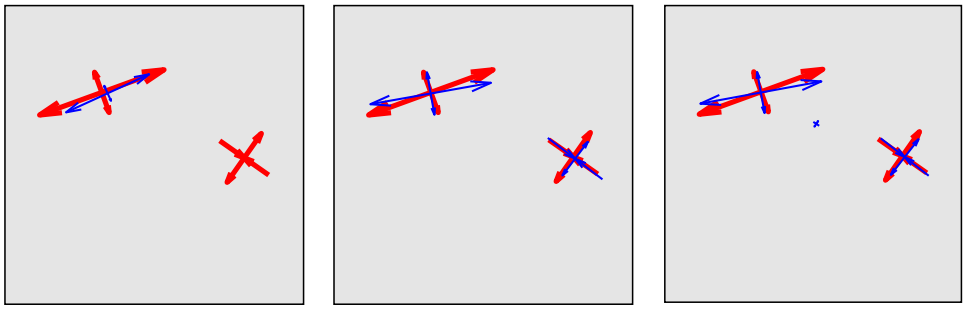
Event	$\ell^{-1}\widehat{\boldsymbol{x}}$	$\ell^{-1}(\boldsymbol{x}^\star = \boldsymbol{x}_{10}^{\star\prime})$	$\widehat{\boldsymbol{M}}(\times 10^3)$	$\boldsymbol{M}^\star(\times 10^3)$
Shear	$\begin{pmatrix} 0.80125 \\ 0.49000 \end{pmatrix}$	$\begin{pmatrix} 0.80135 \\ 0.48999 \end{pmatrix}$	$\begin{pmatrix} 0.000 & 1.600 \\ 1.600 & 0.000 \end{pmatrix}$	$\begin{pmatrix} -0.003 & 1.605 \\ 1.605 & -0.004 \end{pmatrix}$
Tensile	$\begin{pmatrix} 0.32438 \\ 0.70937 \end{pmatrix}$	$\begin{pmatrix} 0.32446 \\ 0.70935 \end{pmatrix}$	$\begin{pmatrix} 2.767 & 0.588 \\ 0.588 & 1.149 \end{pmatrix}$	$\begin{pmatrix} 2782 & 0.585 \\ 0.585 & 1.154 \end{pmatrix}$

3.2 Robustness to noisy data and unknown number of sources

To assess the robustness of the proposed inversion strategy under realistic conditions, we consider the reconstruction of two off-grid events (one tensile and one shear) from hydroacoustic data affected by modeling noise. The measurements are collected at six sensors using five sampled frequencies. Material heterogeneity is introduced by perturbing the solid's Lamé parameters with spatially distributed Gaussian noise of amplitude $\eta = 10\%$, resulting in approximately 40% relative error in the hydroacoustic data. In this experiment, the true number of sources $\widehat{N} = 2$ is assumed unknown. The inversion is performed for increasing trial values $N \in \{1, 2, 3\}$ to evaluate the algorithm's ability to recover the correct number of significant events. As shown in Fig. 4, the case $N = 1$ identifies only one event, while $N = 2$ successfully reconstructs both. When $N = 3$, the same two events are retrieved, with a third negligible source emerging as a numerical artifact. These results confirm that the method remains accurate and stable under high noise levels and model uncertainty, and can infer the correct number of active sources without prior knowledge.

4 Conclusions

This work presented a numerical study on the reconstruction of transient microseismic events in a solid medium immersed in a fluid, based solely on multifrequency hydroacoustic pressure observations. The proposed method aims at recovering both the locations and moment tensors of dipole- and double-couple-type sources, and is motivated by applications such as monitoring reaction-driven cracking in submerged geologic formations. The inverse problem was tackled by combining a frequency-domain forward model for the solid-fluid system with a grid-based combinatorial search over candidate source locations, followed by sequential global and local grid refinements. Numerical results confirmed the effectiveness of the proposed strategy in reconstructing multiple off-grid events under realistic conditions, including sparse sensing and high levels of modeling and data noise. In particular, we demonstrated that the combined use of multi-frequency data and adaptive spatial refinement enables



(a) $N = 1$ (b) $N = 2$ (c) $N = 3$

Figure 4. Off-grid events, noisy data ($\eta = 10\%$): event reconstruction using six sensors and five sampled frequencies ($J = 5$) assuming the *a priori* number of microseismic events $N \in \{1, 2, 3\}$. The "true" and reconstructed moment tensors (as localized) are indicated in red and blue, respectively.

high-resolution source characterization, even when the number of sources is unknown. The results highlight the interplay between spatial and temporal aperture, showing that the lack of one can be partially compensated by the abundance of the other.

References

[1] G. Manthei and K. Plenkers. Review on in situ acoustic emission monitoring in the context of structural health monitoring in mines. *Applied Sciences*, vol. 8, pp. 1595, 2018.

[2] A. Okoli, O. Kolawole, C. Akaolisa, D. Ikoro, and O. Ozotta. Alterations in petrophysical and mechanical properties due to basaltic rock-CO2 interactions: comprehensive review. *Arabian Journal of Geosciences*, vol. 17, pp. 1–23, 2024.

[3] A. Carpinteri, J. Xu, G. Lacidogna, and A. Manuello. Reliable onset time determination and source location of acoustic emissions in concrete structures. *Cement and Concrete Composites*, vol. 34, pp. 529–537, 2012.

[4] K. Ono. *Acoustic Emission*, pp. 1209–1229. Springer, 2014.

[5] M. Ohtsu. Acoustic emission theory for moment tensor analysis. *Research in Nondestructive Evaluation*, vol. 6, n. 3, pp. 169–184, 1995.

[6] K. Aki and P. Richards. *Quantitative Seismology*. University Science Books, Sausalito, California, 2009.

[7] F. Gilbert. Derivation of source parameters from low-frequency spectra. *Philosophical Transactions of the Royal Society of London. Series A, Mathematical and Physical Sciences*, vol. 274, pp. 369–371, 1973.

[8] A. Fichtner and S. Simutė. Hamiltonian monte carlo inversion of seismic sources in complex media. *Journal of Geophysical Research: Solid Earth*, vol. 123, n. 4, pp. 2984–2999, 2018.

[9] J. Labuz, S. Cattaneo, and L.-H. Chen. Acoustic emission at failure in quasi-brittle materials. *Construction and Building Materials*, vol. 15, pp. 225–233, 2001.

[10] F. Lebert, S. Bernardie, and G. Mainsant. Hydroacoustic monitoring of a salt cavity: an analysis of precursory events of the collapse. *Natural Hazards and Earth System Sciences*, vol. 11, n. 9, pp. 2663–2675, 2011.

[11] H. Fan, S. Tariq, and T. Zayed. Acoustic leak detection approaches for water pipelines. *Automation in Construction*, vol. 138, pp. 104226, 2022.

[12] I. Bashir, J. Walsh, P. Thies, S. Weller, P. Blondel, and L. Johanning. Underwater acoustic emission monitoring–experimental investigations and acoustic signature recognition of synthetic mooring ropes. *Applied Acoustics*, vol. 121, pp. 95–103, 2017.

[13] A. Amad, A. Novotny, and B. Guzina. On the full-waveform inversion of seismic moment tensors. *International Journal of Solids and Structures*, vol. 202, pp. 717–728, 2020.

[14] A. Da Silva, A. Novotny, A. Amad, and B. Guzina. Full-waveform reconstruction of micro-seismic events via topological derivative approach. *Journal of Computational Physics*, vol. 510, pp. 113099, 2024.

[15] P. B. Kelemen, R. Aines, E. Bennett, S. M. Benson, E. Carter, J. A. Coggon, J. C. De Obeso, O. Evans, G. Gadikota, G. M. Dipple, and others. In situ carbon mineralization in ultramafic rocks: Natural processes and possible engineered methods. *Energy Procedia*, vol. 146, pp. 92–102, 2018.

[16] J. M. Matter and P. B. Kelemen. Permanent storage of carbon dioxide in geological reservoirs by mineral carbonation. *Nature Geoscience*, vol. 2, n. 12, pp. 837–841, 2009.

[17] F. Hecht. New development in freefem++. *J. Numer. Math.*, vol. 20, n. 3-4, pp. 251–265, 2012.